RSC Advances

ROYAL SOCIETY OF CHEMISTRY

www.rsc.org/advances

Graphical abstract
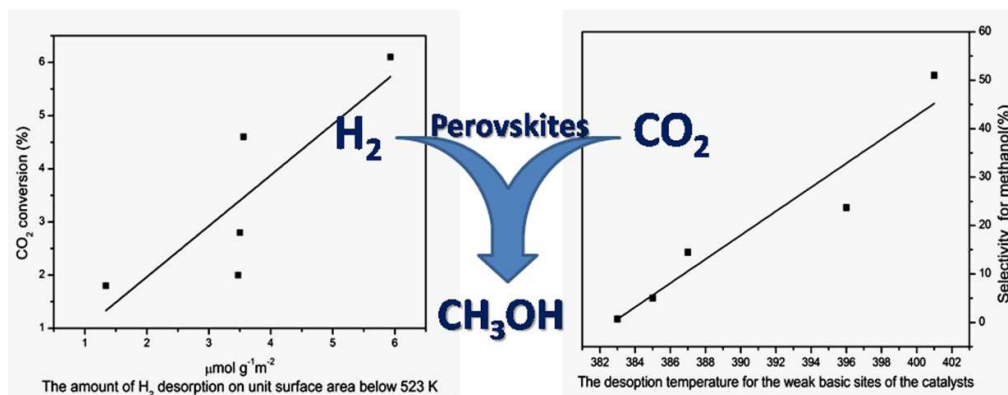
Doped perovskites possess better structure properties, the catalytic performance depends on the behaviour of the reactants.

RSC Advances

ARTICLE

Influence of element doping on La-Mn-Cu-O based perovskite precursors for methanol synthesis from CO$_2$/H$_2$

Haijuan Zhan[a,b], Feng Li[a], Peng Gao[c], Ning Zhao[a,*], Fukui Xiao[a], Wei Wei[a,c],Yuhan Sun[a,d]

Doped La-M-Mn-Cu-O based (M=Ce, Mg, Y, Zn) perovskite materials were prepared by sol-gel method and characterized by XRD, N$_2$-adsorption, ICP-OES, SEM, TPR, N$_2$O-adsorption, XPS and TPD techniques. Upon introduction of the fourth elements, all samples keep the stable LaMnO$_3$ perovskite structure, and part of copper species is separated from the perovskite lattice. More structure defects, lower reduction temperature and better low-temperature H$_2$ adsorption on the unit surface area are observed. In the application for methanol synthesis from CO$_2$/H$_2$, Zn doped catalyst showed better performance which may because that the strength of the weak basic sites play a significant role on methanol selectivity and the amount of H$_2$ adsorbed on unit surface area is the key for CO$_2$ conversion.

1. Introduction

Perovskite-type oxides with the general formula of ABO$_3$ has received much attention because of their important physical properties such as ferro-, piezo-, pyroelectricity, magnetism and electro-optic effects.[1, 2] The perovskite was first applied as catalysts for oxidation of carbon monoxide in 1952-1953 by Parravano.[1] For a typical ABO$_3$ perovskite, A-site is a larger rare earth and/or alkaline earth cation and B-site is a smaller transition metal cation. Fine dispersion of "metal on oxide" catalyst can be obtained by reduction of the perovskite oxides.[3] The advantages of perovskite materials could originate from the ability to accommodate a variety of ions of different valence with appropriate radius that meet

the tolerance factor $t = (r_A + r_B) / \sqrt{2}(r_B + r_O)$ (0.75<t<1).[3,4] The excellent tunable properties make perovskite potential candidate for catalysis.

Recently, the perovskites with AA'BB'O$_3$ structure have been used in catalysis since the substitution of A-site could influence the catalytic performance of B-site.[5] The perovskites with special properties can be obtained by advisable tailoring. At present, the perovskite has been widely studied as the catalyst for NO$_x$, CH$_x$, and CO conversion.[6]

CO$_2$ generated from fossil fuel combustion has led to environmental problem in the form of greenhouse effect and ozone depletion. For the sake of reducing the concentration of CO$_2$ in atmosphere, various strategies have been implemented such as

capture, storage, and utilization of carbon dioxide.[7-10] An important means of carbon dioxide utilization is the hydrogenation reaction. Among the products for carbon dioxide hydrogenation, methanol is considered as the most valuable since it can be used as solvent, alternative fuel and raw material for synthesis of olefins, aromatics or gasoline that derived from traditional petrochemical processes.[11-12]

Many catalytic systems have been employed for methanol synthesis from CO_2 hydrogenation among which Cu-based catalysts have been regarded as most effective.[13] Different promoters have also been investigated such as Zn, Al, Mg, Mn, B, Zr, Y, Ce,[14,15,16] which can improve the catalytic performance via controlling the reactivity of the active site Cu phase by determining texture, exposure of the active sites and interaction pattern with reagents, products and reaction intermediates.[17,18]

Our previous works have found that the Cu-based catalysts from perovskite precursors exhibit better methanol selectivity compared with the other Cu-based catalysts due to the appearance of $Cu^{\alpha+}$ in the structure.[19] The study for CO hydrogenation and CO_2 hydrogenation over $LaMn_{1-x}Cu_xO_3$ perovskite oxides suggested that when the copper amount that substituted manganese was less than or equal to 50%, the $LaMnO_3$ could keep the perovskite structure and show preferable performance for methanol synthesis because of the interaction of Cu^+ and Mn.[20] However, little work

had been conducted on the influence of the fourth metal elements doping for the La-Mn-Cu-O perovskite catalysts. Therefore, in the present work, the La-M-Mn-Cu-O (M=Ce, Mg, Y, Zn) perovskites were prepared and characterized to obtain a clear insight in the influences of the fourth elements doping on the structure and the catalytic performance. The methanol synthesis from CO_2/H_2 was chosen as the model reaction for the perovskite materials to investigate the influence of the structure changing on the catalytic performance.

2. Experimental

2.1 Catalysts preparation

The La-M-Mn-Cu-O (M=Ce, Mg, Y, Zn) pervoskite-type oxides were prepared by sol-gel method using citric acid as complexing agent. The ratio for La, M, Mn, Cu is 0.8: 0.2: 0.5: 0.5. Adequate amounts of the precursor salts ($La(NO_3)_3 \cdot nH_2O$; $Mn(NO_3)_2$, 50% solution; $Y(NO_3)_3 \cdot 6H_2O$; $Cu(NO_3)_2 \cdot 3H_2O$; $Zn(NO_3)_2 \cdot 6H_2O$; $Ce(NO_3)_3 \cdot 6H_2O$; $Mg(NO_3)_2 \cdot 6H_2O$) along with citric acid were dissolved in deionized water at a molar ratio of 2:1 (metal cations: citric acid). The solution was heated to 353 K to remove the water, and then enhanced the temperature to 423 K until ignition. The resulting powder were finally calcined under air at 673 K for 2 h and then at 1073 K for 4 h. The La-Mn-Cu-O catalyst and Mg, Y, Zn, Ce doping catalysts were then denoted as P, Mg-P, Y-P, Zn-P and Ce-P, respectively.

2.2. Characterization of catalysts

X-ray diffraction (XRD) analysis of powered samples was performed using a Panalytica X'Pert Pro X-ray diffractometer with Cu Kα radiation in the range 10° < 2θ < 90° and a scan step of 0.1° min^{-1}.

The surface area of samples was determined by N_2 adsorption-desorption at liquid nitrogen temperature 77.30 K, using a Micromeritics Tristar 3000 instrument. Sample degassing was carried out at 473 K prior to acquiring the adsorption isotherm. The special areas were calculated from the isotherm according to the Brunauer-Emmett-Teller (BET) method.

The dispersion of Cu (D_{Cu}) and exposed Cu surface area (S_{Cu}) were determined by dissociative N_2O adsorption and carried out on Micromeritics AutoChem 2920 instrument. The catalysts (0.15 g) were first reduced in 5 % H_2/Ar mixture (30 mL min^{-1}) for 2 h at 603 K, and the amount of hydrogen consumption was denoted as X. Then, the reduced samples cooled to 338 K and isothermally purged with Ar for 30 min, after which the sample was exposed to N_2O (85 mL min^{-1}) for 1 h to ensure all the metallic copper change into cuprous oxide ($N_2O+Cu{\rightarrow}N_2+Cu_2O$). The samples were then flushed with Ar to remove the N_2O and cooled to room temperature. Finally, a pulse of pure H_2 was passed over the catalyst at 603 K. The surface Cu_2O were reduced in the pulse of pure H_2, and the amount of consumed H_2 was denoted as Y. The dispersion of Cu and exposed Cu surface area of the catalyst were calculated by the Eq (1) [21] and Eq (3) [22]

$$D_{Cu} = \frac{2Y}{X} \times 100\% \qquad (1)$$

$$n_{Cu} = 2Y \qquad (2)$$

$$S_{Cu} = (n_{Cu} \times N)/(1.4 \times 10^{19} \times W)(m^2 g^{-1}) \qquad (3)$$

Where D_{Cu} is the dispersion of Cu, W is the weight of the reduced catalyst, S_{Cu} is the exposed copper surface area per gram catalyst, n_{Cu} is molar number of copper, N is the Avogadro's constant (6.02×10^{23} atoms mol^{-1}), and 1.4×10^{19} is the number of copper atoms per square meter.[21,22]

The elemental composition was determined by inductively coupled plasma optical emission spectroscopy (ICP-OES, Thermo iCAP 6300), 100 mg of the each catalyst was dissolved in 5% HCl solution and diluted. The reference solutions were prepared with the metal nitrates or standard metal oxides used in the catalyst preparation.

Investigations of the sample microstructure morphology were performed on a FETXL30 S-FEG scanning electron microscope (SEM) with an accelerating voltage of 10.0 kV.

X-ray photoelectron spectroscopy (XPS) analyses were performed over a Kratos XSAM800 spectrometer equipped with Al Kα radiation (12 kV × 15 mA, hv = 1486.6 eV) under ultrahigh vacuum (10^{-7} Pa). The binding energies were calibrated internally by adventitious carbon deposit C(1s) with E_b= 284.6 eV (accuracy within ±0.1 eV). Samples were treated under pure hydrogen at 603

K for 2 h in the pre-treatment chamber before transferred to the analysis chamber.

Temperature program reduction (TPR) measurements were carried out in order to determine the reducible species and performed in a U-tube quartz reactor. The samples (50 mg) were purged with Ar (30 mL min^{-1}) at 423 K to remove physically adsorbed water and then reduced in the flow of 5 vol.% H_2+Ar (30 mL min^{-1}) at a heating rate of 5 K min^{-1} up to 873 K. Thermal conductivity detector (TCD) was used to monitor the consumption of H_2.

The adsorption property of H_2 for the studied sample was measured by H_2 temperature-programmed desorption (H_2-TPD). The catalyst was first reduced at 603 K and cooled to 318 K to saturate for 60 min in H_2 flow of 30 mL min^{-1} for 2 h. Then the catalyst was flushed with Ar flow (40 mL min^{-1}) to remove all physical adsorbed molecules. Afterward, the TPD experiment was started with a heating rate of 10 K min^{-1} under Ar flow (40 mL min^{-1}), and the change of hydrogen signal was monitored by a TCD and quantitatively calibrated by H_2 pulses.

The basicity of the catalyst was measured by CO_2 temperature-programmed desorption (CO_2-TPD) was performed in the same way as that of H_2-TPD; the only difference was that the desorbed CO_2 was detected by a BALZER mass spectrometer. CO_2 peak area was quantitatively calibrated by injecting CO_2 pulses.

2.3. Evaluation of catalysts

Activity measurements in the hydrogenation of CO_2 were carried out in a continuous-flow, high-pressure, fixed-bed reactor. Catalyst (1.5 g, 40-60 mesh) diluted with quartz sand (60 mesh) was placed in a stainless steel tube reactor. Prior to reaction, the catalyst was reduced in pure H_2 at a flow-rate of 80 mL min^{-1} under atmospheric pressure. The reduction temperature was programmed to increase from room temperature to 603 K at a heating rate of 1 K min^{-1} and maintained at 603 K for 8 h. The reactor was then cooled to room temperature. After reduction, the activities of the catalyst samples in CO_2 hydrogenation process were determined under reaction conditions of 523 K, 5.0 MPa, n(H_2):n(CO_2)=3:1, GHSV=4000 h^{-1}. The steady-state activity measurements were taken after at least 24 h on the stream. Products were quantitative analyzed with gas chromatograph equipped with a TCD, and the columns were TDX-01 for gas of H_2, CO and CO_2 and the Propake-Q for liquid of water and methanol. The CO_2 conversion and the carbon-based selectivity for CH_3OH, CO and CH_4 were calculated by an internal normalization method. The space time yields (STYs) of CH_3OH, which gave the amounts of CH_3OH produced per gram catalyst per hour, were defined as the Eq (4):

$$STY_{CH_3OH} = \frac{W_T \times X\,(CH_3OH)}{t \times m} \qquad (4)$$

Where W_T was the total weight of CH_3OH and H_2O product (g); X(CH_3OH) was the mass fraction of

CH$_3$OH; t was the reaction time (h) ; m was the weight of catalyst (g).

3. Results and discussion

3.1 Textural and structural properties

The X-ray diffraction patterns of the fresh and reduced perovskites are presented in Fig.1 a and b respectively. It can be seen that the LaMnO$_3$ (JCPDS # 75-0440) are the main phase for all samples. The diffraction peak at about 2θ=32.5° shift towards higher values with the addition of the fourth elements. According to the Bragg formula, $n\lambda=2d\sin\theta$ (where d denotes the crystalline plane distance for indices (h k l), λ is the X-ray wavelength and θ is the diffraction angle), the d value will decrease when the ions with large radii are substituted by those with small radii (1.36 Å for La^{3+}, 1.34 Å for Ce^{3+}, 1.08 Å for Y^{3+} , 0.74 Å for Zn^{2+}, 0.73 Å for Cu^{2+}, 0.72 Å for Mg^{2+}, 0.65 Å for Mn^{3+}), which results in the shifts of the diffraction peaks to higher values.[23,24] The result implies that the fourth elements have strong influences on La. Since the Mg^{2+} is slightly smaller than Cu^{2+}, it might also have a complex effect on perovskite structure. For P sample, only LaMnO$_3$ phase is observed which means that all the copper either penetrates into the pervoskite structure or well dispersed on the catalyst.[20] With the addition of other ions, small peaks at 2θ=35.6° and 38.9° assigned to CuO (JCPDS # 89-5899) appear and the intensity of the diffraction peak of the LaMnO$_3$ phase increase in the order of: Mg-P < Ce-P < Y-P < P < Zn-P. The strength of the CuO peak is in the order of: Y-P < Ce-P < Zn-P < Mg-P, which suggests the influence on the perovskite structure with the introduction of the fourth elements. When Mg is introduced, the strongest diffraction peak of CuO and the weakest diffraction peak of LaMnO$_3$ are found which implies the stronger impact of Mg for the penetration of copper into the catalyst lattice as well as the perfection of LaMnO$_3$ in comparison with other elements. As Mg has the similar radius with Cu, it could have effect on both A-site and B-site of the perovskite oxide. However, doping with Y in the sample has little influence i.e. the characters of Y^{3+} are almost the same with La^{3+} which then lead to little disturbance for the catalyst structure. With the doping of Zn, the strongest diffraction peak of LaMnO$_3$ is observed which suggests that the perovskite structure tends to perfection due to the similar radius, valence state and electronegativity for Zn and Cu. In all diffraction patterns, no phases that ascribe to Mg, Y or Zn is observed while a new phase ascribed to CeO$_2$ is found for the sample of Ce-P which demonstrates that it is difficult for all the Ce to enter the perovskite lattice which agrees with the conclusion by Weng et al..[25]
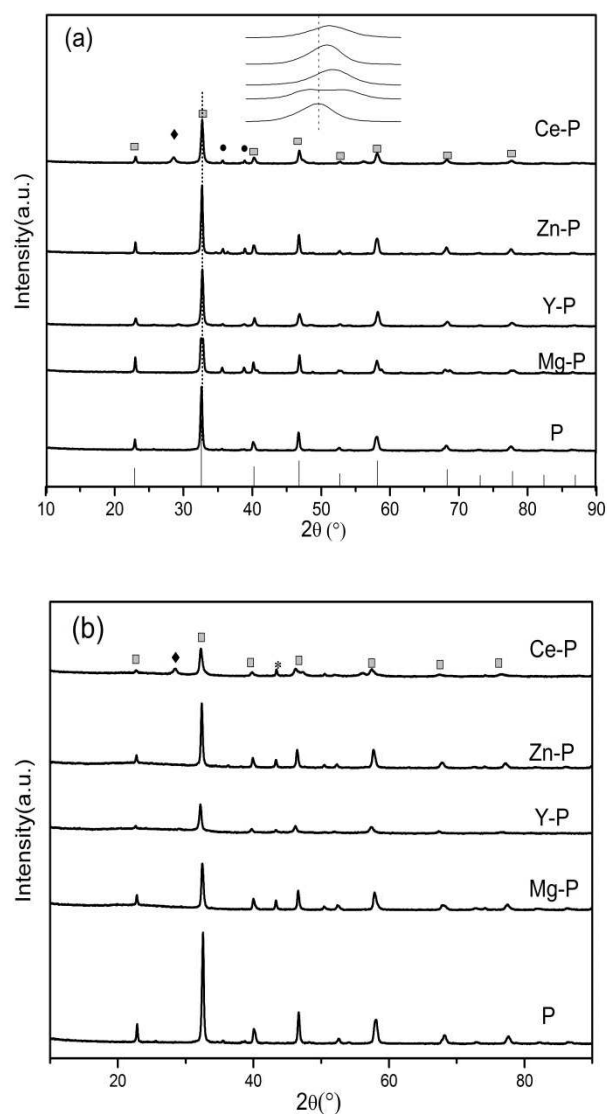
Fig.1. XRD patterns of the calcined (a) and reduced (b) perovskite-type catalysts: (□) $LaMnO_3$; (●) CuO; (♦) CeO_2; (*) Cu.

As shown in Fig.1-b, for all reduced samples, $LaMnO_3$ phase is still the main phase while the CuO phase disappears and the Cu phase emerges which reveals that the reduction process does not destroy the perovskite structure. However, the perovskite structure has undergone some changes,

e.g. the phase symmetry of all samples has changed except for P (Table 1). It is interesting that the reduction process leads to ordered $LaMnO_3$ phase only for Mg-P. The transition may occur in several steps and the deviation from the cubic perovskite structure may proceed from a simple distortion of the cubic unit cell, or an enlargement of cubic unit cell, or a combination of both.[3] Moreover, the less particles shrink for Mg doped sample may result from the electronic property of alkaline-earth metals.

The physicochemical properties of the calcined perovskite-type catalysts are also summarized in Table 1. The Y-P and the Zn-P possesses the largest and the lowest specific surface area, respectively. Moreover, the exposed Cu surface area and the Cu dispersion are measured by N_2O adsorption technique. The largest copper surface area is observed for Y-P, nevertheless, the copper surface area cannot be measured for both P and Ce-P. Since the surface copper may have strong influence on the activity for CO_2 hydrogenation reaction,[26] the lower copper surface area may not favorable for the conversion of CO_2. The ICP results show that the real contents of the samples are similar to the nominal values. For all catalysts, the experimental lanthanum amount is lower than the theoretical value.

Table 1

The phase symmetry, lattice parameters and the physiochemical properties of the calcined perovskite-type catalysts

Samples	Phase symmetry	Size of $LaMnO_3$ crystallites (Å)	Elemental composition (ICP-OES)[a]	S_{BET} ($m^2 g^{-1}$)	Dispersion (%)[b]	S_{Cu} ($m^2 g^{-1}$)

	Calcined	Reduced	Calcined	Reduced				
P	cubic	cubic	418	290	$La_{0.84}Mn_{0.51}Cu_{0.50}$	6.5	-	-
Mg-P	orthorhombic	cubic	206	332	$La_{0.67}Mg_{0.22}Mn_{0.49}Cu_{0.50}$	5.4	0.9	1.2
Y-P	cubic	hexagonal	378	316	$La_{0.67}Y_{0.23}Mn_{0.47}Cu_{0.50}$	11.3	3.8	4.6
Zn-P	cubic	orthorhombic	467	462	$La_{0.67}Zn_{0.18}Mn_{0.50}Cu_{0.50}$	4.1	0.7	0.9
Ce-P	cubic	orthorhombic	333	238	$La_{0.68}Ce_{0.19}Mn_{0.49}Cu_{0.50}$	7.2	-	-

[a] Subscripts came from ICP results

[b] Calculated from N_2O dissociative adsorption.

Fig.2 shows the SEM images of the prepared catalysts. The results show that all samples present as irregular granules. Compared with other samples, the particle size is smaller for Y-P and P. Particle agglomeration is observed for Mg-P and Ce-P while not for Zn-P in spite of the large particles.
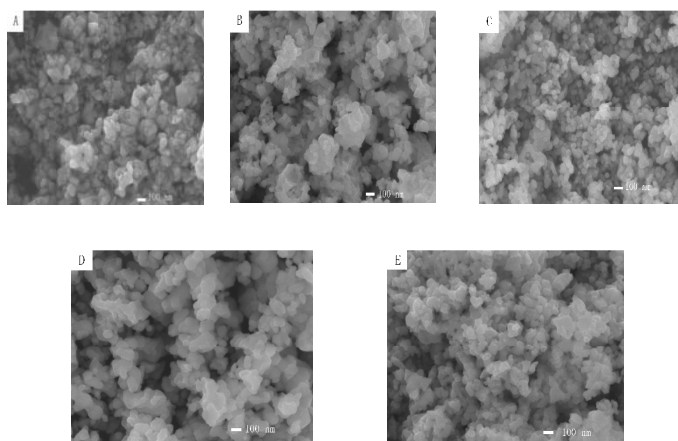

Fig.2. SEM images of the calcined catalysts (A) P，(B) Mg-P，(C) Y-P，(D) Zn-P, (E) Ce-P

3.2 The XPS investigations

The reduced perovskite-type catalysts are analyzed by XPS, and the binding energies (BE) of La $3d_{5/2}$, Mn 2p and O1s are presented in Table 2. The La $3d_{5/2}$ peak at around 834.3 eV is close to the value of pure lanthana at 834.4 eV, indicating that lanthanum ions are present in the trivalent form.[27] However, with the addition of the fourth elements, the BE of La $3d_{5/2}$ shift towards lower values which implies the increasing of the electron cloud density around La ions. It may due to the fourth elements affect the transfer of the electrons of La to O since O has the highest electronegativity value among all elements.[28]

For O 1s, the lower binding energy at around 528.9-529.1 eV can be ascribed to the lattice oxygen (O^{2-})[15,28] and the BE value at around 530.8-533.0 eV is assigned to the adsorbed oxygen species(O_{ad}) in the surface which contains hydroxyl (OH^-), carbonate species (CO_3^{2-}) and molecular water. Doped with the fourth components, the binding energy decreases which indicates that there are more electrons around oxygen. It is likely that the fourth components transfer the electronic to the oxygen. Obviously, the intensity of the peaks is different from each other. The presence of surface adsorbed oxygen species suggests the formation of oxygen vacancies in the defected oxides.[29] The increasing of the O_{ad}/O^{2-} ratio upon addition of the fourth elements indicates that the increasing of the

amount of defect on perovskite oxide that is favorable for the activation of the catalyst. The binding energy of Mn $2p_{3/2}$ for MnO, Mn_2O_3 and MnO_2 are located at 640.6, 641.9 and 642.2 eV respectively. As reported in other studies,[30,31] the mean oxidation state of Mn ions at the surface layers is extremely difficult to detect by XPS. However, the previous reports suggested that the BE difference between $Mn2p_{3/2}$ and O1s increase with about 0.6-0.7 eV for the change of the oxidation state between Mn^{3+} and Mn^{4+}. In this study, as shown in Table 2, the BE difference is in the range of 112.3-113.0 eV which means a change of the Mn^{4+}/Mn^{3+} ratio.[32,33]

Since the binding energy of the Cu $2p_{3/2}$ band in the metal (932.6 eV) and in Cu^+ (932.4 eV) are almost same, they can be distinguished by different kinetic energy of the Auger Cu LMM line position in Cu^0 (918.6 eV), Cu^+ (916.7 eV) or in Cu^{2+} (917.9 eV).[26,34] The Auger electron spectroscopies of Cu LMM of reduced samples are shown in Fig.3. The profiles are deconvoluted into two peaks. It can be seen that the majority of the copper species exist as Cu^+ for all samples except for the P sample. The predominance of Cu^+ in P is in accordance with the report of Jia et al.[20] and the results of XRD and N_2O-adsoption mentioned above. The weak

Cu^0 peak could be the explanation for the immeasurable of exposed Cu^0 in the N_2O-adsoption results for Ce-P (Table 1).
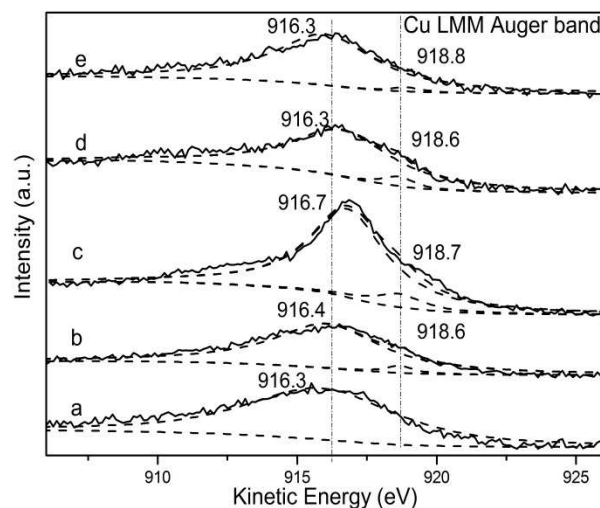

Fig.3. Cu LMM Auger electron spectroscopy of (a) P; (b)Mg-P; (c) Y-P; (d) Zn-P; (e) Ce-P samples after reduction.

The surface compositions and the nominal concentration of the catalysts are also listed in Table 2. The enrichment of Cu and depletion of La and Mn are observed for P. However, the Mn enrichment is found with the doping of the fourth elements. As Y and Ce entered the perovskite structure, it may lead to further enrichment of Cu on the catalyst surface. For Zn-P, the lack of both Zn and Cu on the surface may indicate that more Zn and Cu enter the bulk of the sample. It is also found that Mg is greatly enriched on the surface of Mg-P.

Table 2

The binding energy of La, Mn, O, the ratio of different oxygen species and relative surface concentration of metals.measured by XPS.

Binding energy (eV)		Relative suface conentration of metal(%)[a]

Samples	La $3d_{5/2}$ (eV)	Mn $2p_{3/2}$ (eV)	O 1s (eV)	O_{ad}/O^2	La(%)	Mn (%)	Cu(%)	M (%)
P	835.1	642.2	529.2 (50.5%)	1.02	46.7 (50)	22.2(25)	31.1(25)	-
			531.7 (49.5%)					
Mg-P	834.0	642.0	529.1 (51.5%)	1.06	25.3(40)	28.7(25)	25.6(25)	Mg: 20.4(10)
			531.5 (48.5%)					
Y-P	834.4	641.3	529.0 (54.0%)	1.18	26.1(40)	28.9(25)	32.7(25)	Y: 12.3(10)
			531.4 (46.0%)					
Zn-P	834.1	641.5	529.1 (51.2%)	1.05	38.5(40)	31.5(25)	21.3(25)	Zn: 8.7(10)
			531.5 (48.8%)					
Ce-P	834.3	641.8	529.2 (51.9%)	1.08	28.3(40)	27.8(25)	31.4(25)	Ce: 12.5(10)
			532.2 (48.1%)					

[a] Values in parentheses are nominal concentration normalized to the total metal content

Fig.4. shows the binding energy curves of the fourth components. The peak at 49.4 eV is attributed to Mg-O binding,[35] 1021.8 eV is assigned to Zn-O binding.[30] While the 156.8 eV and 158.6 eV may originate from the Y existed as 3+.[36] For Ce-P, six peaks located at 882.3, 888.4, 898.1, 900.7, 907.2 and 916.2 eV can be ascribed to Ce^{4+} which is in accordance with the XRD result of the Ce-P.[37]

3.3 The reducibility of the prepared catalysts

The TPR profiles of all samples are shown in Fig.5. It can be seen that the Y-P sample has two reduction peaks (denoted as peak α and peak β) while other samples present only one peak (denoted as peak β) which indicates that there is only one kind of copper spices in the P, Mg-P, Zn-P and Ce-P samples. The peak α at the lower temperature can be attributed to the reduction of highly dispersed surface copper species, whereas the peak at higher temperature is related to the reduction of the bulk-like copper species.[38] Upon introduction of the fourth elements, the enrichment of the copper on the surface (Table 2) leads to lowered reduction temperature. Moreover, more O_{ad} (Table 2) on the surface may also result in lowered reduction temperature which confirms the function of the defection in the perovskites. Y doping can increase the amount of the copper on the surface area which agrees with the N_2O chemisorption.

The H_2 consumption in the TPR experiment is listed in Table 3. The amount of H_2 consumption is in the order of: Zn-P > Y-P > P > Mg-P > Ce-P, which indicates that there are more copper species that can be reduced for Zn-P and Y-P.
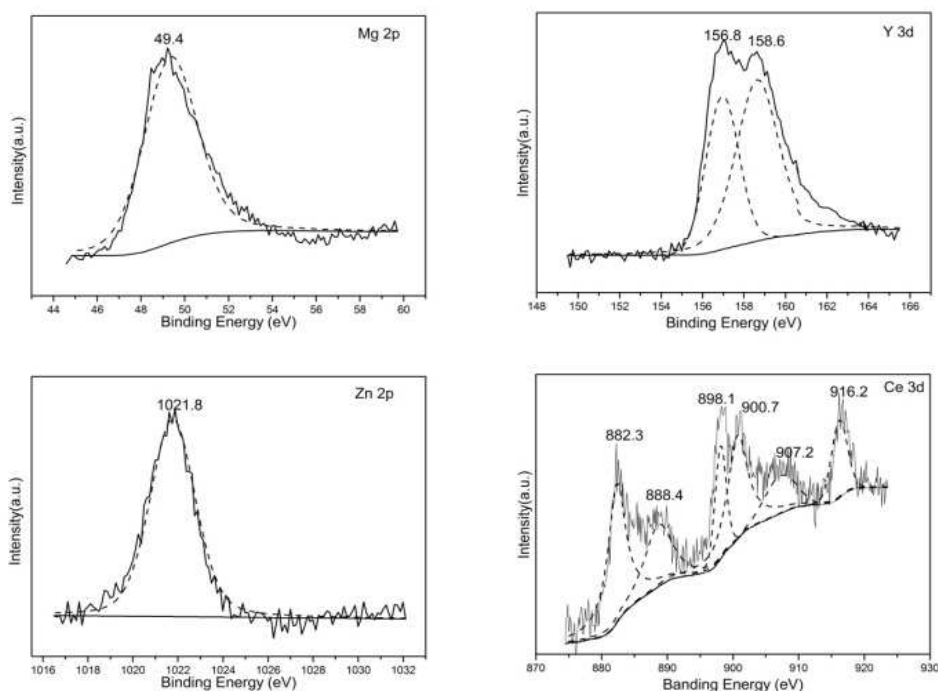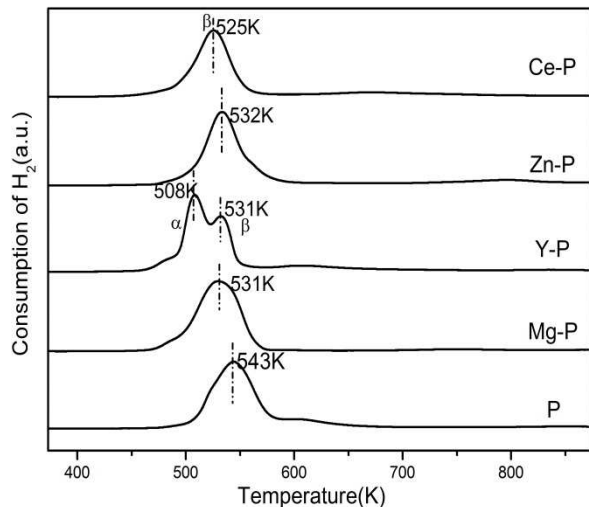
Fig.4. XPS results of Mg2p, Y3d, Zn3d and Ce3d.

Fig.5. TPR profiles of the catalysts.

Table 3

The H_2 consumption amount in TPR and the H_2 desorption amount in H_2-TPD experiment.

Samples	H_2 consumption (mmol g-1)	H_2 desorption (µmol g-1)				
		Peak α	Peak β	Total	H_2 -523[a]	H_2 -523[b]
P	9.47	48.2	165.2	213.4	8.7	1.34
Mg-P	9.06	50.6	68.3	118.9	18.9	3.50
Y-P	9.50	60.7	76.8	137.5	40.2	3.56
Zn-P	9.59	35.5	46.8	82.3	24.3	5.93
Ce-P	8.65	69.3	51.6	120.9	25.0	3.47

[a] H_2 desorption below 523 K

[b] H_2 desorption below 523 K on per unit are (µmol g^{-1}m^{-2})

3.4 H_2-TPD analysis

The H_2-TPD profiles of the reduced catalysts are shown in Fig.6. In order to get more insight into the H_2-TPD results, the profiles are deconvoluted into two Gaussian peaks. According to the literature, the lower peak around 400 K can be assigned to the desorption of weakly molecularly adsorbed hydrogen on the Cu^0 sites. However, such desorption peak are not observed because of less surface content of Cu^0. The desorption peak (peak α) at lower temperature can be assigned to the

desorption of dissociative hydrogen on the surface copper species, while the higher temperature peak (peak β) can be ascribed to desorption of strongly adsorbed dissociative hydrogen on the bulk copper or other metal oxides.[39-41] It can be seen that the desorption peak of H_2 at low temperature shifts toward even lower temperature with the introduction of the fourth components. However, the temperature of the peak β is higher than that for methanol synthesis, which means that these hydrogen might have little effect on the reaction. In addition, the desorption peak of the H_2 presents as a broad peak also suggests the strong spillover in the perovskite catalysts.

The amount of H_2 desorption over the pre-reduced materials is also listed in Table 3. With the introduction of the fourth elements, the total and high temperature desorption amount of hydrogen decreased. However, the desorption amount of H_2 at low temperature increased except Zn-P. It implies that the doping of the fourth element is not favor the desorption of H_2, especially under high temperature. Moreover, the H_2 desorption on the unit surface area below 523 K (test temperature) increased for all the four components samples.
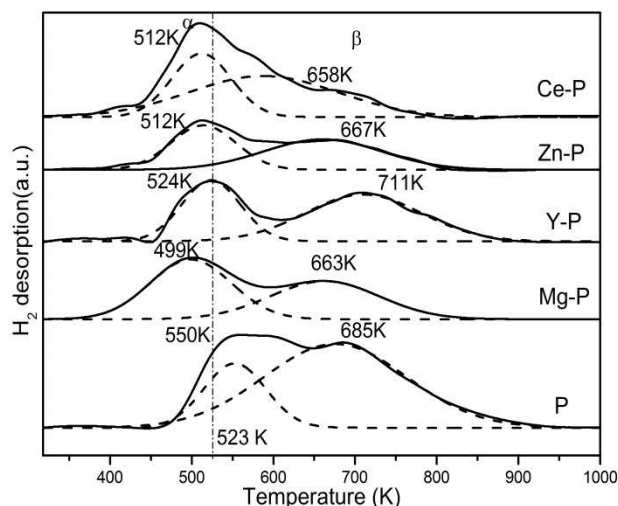

Fig.6. H_2-TPD curves of the catalysts.

3.5 CO_2-TPD analysis

Two desorption peaks (denoted as peak α and peak β) are observed for all samples (Fig.7) which could be assigned to weak basic sites (around 400 K) and strong basic sites (around 600 K). The weak basic sites may be ascribed to the linear adsorption of CO_2 while the strong basic sites may result from the bridge adsorption of CO_2.[41] With the introduction of the fourth components, the peak α shifts to higher temperature which indicates the increasing of the strength of the weak basic sites. The strength for the weak basic sites of the catalysts increases in the order of: P < Ce-P < Y-P< Mg-P < Zn-P. However, the peak β shifts to lower temperature which reveals that the addition of the fourth elements decrease the basicity of the strong basic sites of the samples.

Doping with the fourth elements leads to the change of the amount of the basic sites. The quantitative analysis for the CO_2-TPD based on the relative area of the profiles is listed in Table 4, in

which the P sample is assigned as 1.00. For Mg-P, the amount of all basic sites increases due to the alkalinity of Mg. Although the amount of total basic sites and strong basic sites for Y-P increases, the amount of weak basic sites decreases. Moreover, the amount of the weak basic sites increases for Zn-P and Ce-P samples despite the decrease of the amount of the strong basic sites and total basic sites.
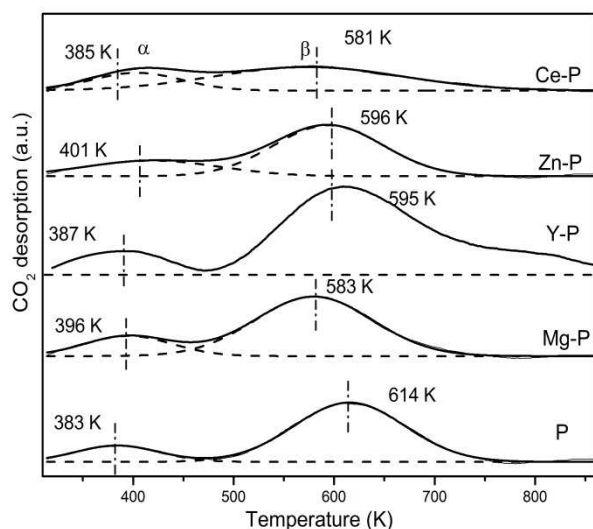

Fig.7. CO_2-TPD curves of the catalysts.

Table 4

The basicity calculated from CO_2-TPD data.

Samples	Adsoption type and distribution based in CO_2-TPD data[a]		
	Peak α	Peak β	Total
P	1.00 (383)	1.00 (614)	1.00
Mg-P	1.30 (396)	1.06 (583)	1.11
Y-P	0.87 (387)	1.67 (595)	1.53
Zn-P	1.56 (401)	0.85(596)	0.97
Ce-P	1.22 (385)	0.69(581)	0.78

[a] The amount of basicity of P is assigned as 1.00 tocompare with other samples and the values in parentheses are the desorption temperature (K).

3.6 Catalytic performance

The catalytic performances of the catalysts for CO_2 hydrogenation to methanol are summarized in Table 5. The main product is methanol and the by-products are CO and H_2O derived from reverse water gas shift (RWGS) reaction.[34,38,42] It is found that the CO_2 conversion and methanol selectivity are improved for the doped catalysts. With the introduction of Zn, both the CO_2 conversion and the methanol selectivity increased greatly which might due to the fact that CO_2 could be activate on the site of Cu^+-O-Zn.[43,44] However, the addition of Ce leads to a slight improvement for the catalytic performance. The relationship between the CO_2 conversion and the amount of H_2 desorption on unit surface area below 523 K (Table 3) is shown in Fig.8. It can be seen that the more H_2 desorbed on the unit area, the more CO_2 conversion. Lower CO_2 conversion may result from lower copper content as well as lower surface area of copper in the system. The results of Fig.9 indicate that the strength of the weak basic sites play an important role for methanol selectivity. The formate theory may explain the relationship between the catalytic performance and the H_2 desorption as well as the strength of the weakly basic sites in which the formaldehyde is the intermediate species and the basic sites is the key factor for methanol selectivity.[43]

Table 5

The performance for methanol synthesis from CO_2 hydrogenation over the reduced catalysts.

Samples	CO_2 conversion (%)	Selectivity (C-mol%)		
		CH_3OH	CO	CH_4
P	1.8	0.7	93.4	5.9
Mg-P	2.8	23.7	68.1	6.5
Y-P	4.6	14.5	82.6	2.9
Zn-P	6.1	51.0	46.4	2.7
Ce-P	2.0	5.0	85.9	9.2

Reaction conditions: $n(H_2)/n(CO_2)$=3:1, T=523 K, P=5.0 MPa, GHSV=4000 h^{-1}.

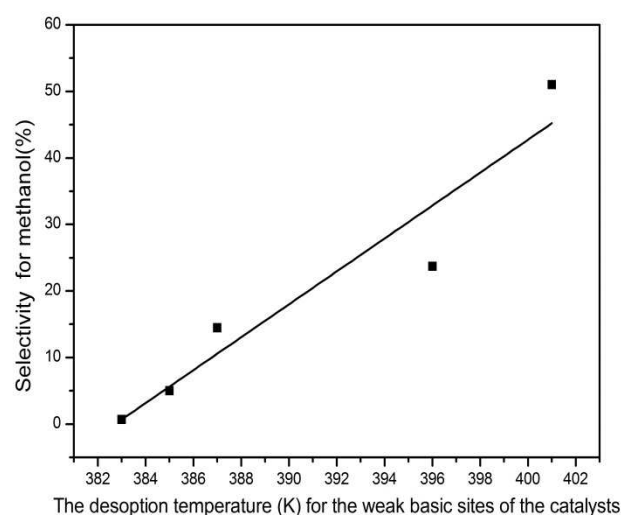**Fig.9.** The relationship between the selectivity for methanol and the strength of the weak basic of the catalysts.

Fig.8. The relationship between the CO_2 conversion and the amount of H_2 desorbed on unit surface area below 523 K.

Previous studies have demonstrated that two active centers were involved in the catalytic process of CO_2 hydrogenation for Cu-based catalysts which undergo the formate intermediate process,[26,45] i.e. CO_2 was adsorbed on the surface of the metal oxides such as ZnO and ZrO_2 while the H_2 was adsorbed on the Cu sites. Then the activated species participated in the reaction to produce the aim products.[43,46,47] During the reaction, either methanol or by-product CO was produced from the intermediate, formate species, and the strength of the basic sites decided the products selectivity. With the special perovskite structure, in our study, CO_2 could be adsorbed on the basic sites (perovskite oxide carriers) to form activated CO_2^* and H_2 may be adsorbed and activated on the Cu sites resulting from the reduction of extra-perovskite and intra-perovskite copper species. The methanol selectivity is only related to the strength of the weak basic sites. The hydrogen supplied

from Cu sites may spillover to the basic sites and react with the CO_2^* to form the formate intermediate. The formate species formed on the weak basic sites may lead to methanol production, while the intermediate formed on other basic sites may produce CO. The possible reaction mechanism for CO_2 hydrogenation to methanol over the perovskites catalysts can be described in Scheme 1.
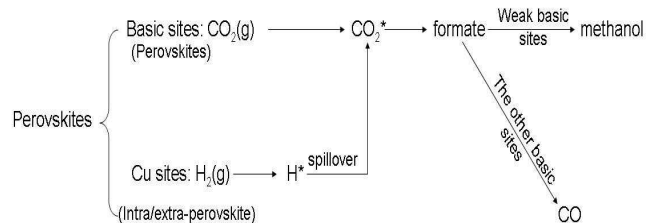
Scheme 1. Proposed reaction mechanism of CO_2 hydrogenation to methanol over the perovskite catalysts.

4. Conclusions

Doped La-M-Mn-Cu-O (M=Ce, Mg, Y, Zn) catalysts derived from perovskite-type precursors were prepared by sol-gel method. Introduction of the fourth elements leads to the separation of copper out of the $LaMnO_3$ perovskite lattice and thus produces more oxygen vacancies. Lower reduction temperature and low temperature adsorption properties are obtained with the increasing of defects for the doped samples. For the reaction of CO_2 hydrogenation to methanol, the CO_2 conversion increases with increasing of the amount of absorbed H_2 on the unit area under 523 K, while the methanol selectivity increases upon increasing of the strength of the weak basic sites. Both the H_2 adsorption amounts on the unit area and weak basic site strength are enhanced

considerably as a result of the introduction of Zn such that improved the catalytic performance. Firstly, the Zn doped sample showed the largest H_2 consumption in the TPR result which indicated the existence of the most amount of reducible copper (the active site for the reaction) in the sample. Secondly, the Zn doped sample possessed the maximum amount of H_2 desorption on the unit surface area under 523 K. Thirdly, the samples possessed more weakly basic sites which favored the methanol selectivity. The Ce-P shows an iso-conversion compared with P due to the slight improvement of the H_2 adsorption. However, with the slight enhancement of the weak basic sites, the Ce-P showed almost five times more selectivity towards methanol which implies that it is probably much easier to improve the methanol selectivity for the perovskite catalytic system.

Acknowledgments

Notes and references

^{a}State Key Laboratory of Coal Conversion, Institute of Coal Chemistry, Chinese Academy of Sciences, South Taoyuan Road 27#, Taiyuan 030001, People's Republic of China

University of Chinese Academy of Sciences, Beijing 100049,
People's Republic of China
Center for Greenhouse Gas and Environmental Engineering,
Shanghai Advanced Research Institute, Chinese Academy of
Sciences, Shanghai 201203, People's Republic of China
CAS Key Laboratory of Low-carbon Conversion Science and
Engineering, Shanghai Advanced Research Institute, Chinese
Academy of Sciences, Shanghai 201203, People's Republic of China

1. L. G. Tejuca, J. L. G. Fierro and J. M. D. Tascón, *Adcances in Catalysis,*1989, **36**, 237-328.

2. X. F. Sun, S. Komiya and Y. Ando, *Physica C,*2003, **388-389**, 355-356.

3. M. A. Pĕna, J.L.G.Fierro, *Chem. Soc. Rev.* , 2001, 1981-2017.

4. C. C. R. Clive D, and Mark J.Hampden-Smith, *Chem. Soc. Rev.* , 1993, **93**, 1205-1241.

5. J. L. G. Fierro. M. L. Rojas, L.G.Tejuca, A. T. Bell, *J. Catal.* , 1990, **124**, 41-51.

6. J. Zhang, X. Weng, Z. Wu, Y. Liu and H. Wang, *Appl. Catal., B* 2012, **126**, 231-238.

7. B. Li, Y. Duan, D. Luebke and B. Morreale, *Appl. Energy,*2013, **102**, 1439-1447

8. R. Steeneveldt, B. Berger and T. A. Torp, *Chem. Eng. Res. Des.* , 2006, **84**, 739-763.

9. K. M. Yu, I. Curcic, J. Gabriel and S. C. Tsang, *ChemSusChem*, 2008, **1**, 893-899.

10. M. Peters, B. Köhler, W. Kuckshinrichs, W. Leitner, P. Markewitz and T. E. Müller, *ChemSusChem*, 2011, **4**, 1216-1240.

11. K. Damen, M. van Troost, A. Faaij and W. Turkenburg, *Prog. Energy Combust. Sci.* , 2006, **32**, 215-246.

12. G. A. Olah, *Angew Chem Int Ed Engl*, 2005, **44**, 2636-2639.

13. K. C. Waugh, *Catal. Today* 1992, **15**, 51-75.

14. J. Słoczynski, R. Grabowski, P. Olszewski, A. Kozlowska, J. Stoch, M. Lachowska and J. Skrzypek, *Appl. Catal., A* 2006, **310**, 127-137.

15. J. Słoczyński, R. Grabowski, A. Kozłowska, P. Olszewski, M. Lachowska, J. Skrzypek and J. Stoch, *Appl. Catal., A* 2003, **249**, 129-138.

16. F. Meshkini, M. Taghizadeh and M. Bahmani, *Fuel*, 2010, **89**, 170-175.

17. F. Arena, G. Mezzatesta, G.Zafarana, G. Trunfio, F. Frusteri and L. Spadaro, *Catal. Today* 2013, **210**, 39-46.

18. F. Arena, G. Mezzatesta, G.Zafarana, G. Trunfio, F. Frusteri and L. Spadaro, J. *Catal.* 2013, **300**, 141-151.

19. H. J. Zhan, F. Li, P. Gao, N. Zhao, F. K. Xiao, W. Wei, L. S. Zhong and Y. H. Sun, *J. Power Sources,*2014, **251**, 113-121.

20. L. S. Jia, J. Gao, W. P. Fang and Q.B. Li, *J. Rare Earths* 2010, **28**, 747-751.

21. Z. Yuan, L. Wang, J. Wang, S. Xia, P. Chen, Z. Hou and X. Zheng, *Appl. Catal., B* 2011, **101**, 431-440.

22. R. Yang, X. Yu, Y. Zhang, W. Li and N. Tsubaki, *Fuel*, 2008, **87**, 443-450.

23. R.D.Shannon, *Acta Cryst*, 1976, **A32**, 751.

24. J. P. Zou, L. Z. Zhang, S. L. Luo, L. H. Leng, X. B. Luo, M. J. Zhang, Y. Luo and G. C. Guo, *Int. J. Hydrogen Energy* 2012, **37**, 17068-17077.

25. D. Weng, H. Zhao, X. Wu, L. Xu and M. Shen, *Mater. Sci. Eng. A:* 2003, **361**, 173-178.

26. P. Gao, F. Li, H. J Zhan, N. Zhao, F. K. Xiao, W. Wei, L. S. Zhong, H. Wang and Y. H. Sun, *J. Catal.* , 2013, **298**, 51-60.

27. N. Merino, B. Barbero, P. Grange and L. Cadus, *J. Catal.* , 2005, **231**, 232-244.

28. K. Sutthiumporn and S. Kawi, *Int. J. Hydrogen Energy* 2011, **36**, 14435-14446.

29. Z. Li, M. Meng, Y. Zha, F. Dai, T. Hu, Y. Xie and J. Zhang, *Appl. Catal., B* 2012, **121-122**, 65-74.

30. F. Rubio-Marcos, A. Quesada, M. A. García, M. A. Bañares, J. L. G. Fierro, M. S. Martín-Gonzalez, J. L. Costa-Krämer and J. F. Fernández, *J. Solid State Chem.* , 2009, **182**, 1211-1216.

31. Y. H. Kenji Tabata, Eiji Suzuki, *Appl. Catal., A* 1998, **170**, 245-254.

32. N. H. Batis, P. Delichere and H. Batis, *Appl. Catal., A* 2005, **282**, 173-180.

33. H. Najjar and H. Batis, *Appl. Catal., A* 2010, **383**, 192-201.

34. P. Gao, F. Li, N. Zhao, F. K. Xiao, W. Wei, L. S. Zhongand Y. Sun,*Catal. Sci. Technol.*, 2012, **2**, 1447-1454.

35 Y. Aykut, G. N. Parsons, B. Pourdeyhimi and S. A. Khan, *Langmuir*, 2013, **29**, 4159-4166.

36. L. Dusoulier, R. Cloots, B. Vertruyen, J. L. Garcia-Fierro, R. Moreno and B. Ferrari, *Mater. Chem. Phys.* , 2009, **116**, 368-375.

37. A. F. Lucrédio, G. T. Filho and E. M. Assaf, *Appl. Surf. Sci.* , 2009, **255**, 5851-5856.

38. X. Guo, D. Mao, G. Lu, S. Wang and G. Wu, *J. Mol. Catal. A: Chem.* , 2011, **345**, 60-68.

39. X. Dong, H. B.Zhang, G. D. Lin, Y. Z. Yuan and K.R.Tsai, *Catal. Lett.* , 2003, **85**, 3-4.

40. F. Arena, G. Italiano, K. Barbera, G. Bonura, L. Spadaro and F. Frusteri, *Catal. Today* 2009, **143**, 80-85.

41. L. Zhang, Y. Zhang and S. Chen, *Appl. Catal., A* 2012, **415-416**, 118-123.

42 P. Gao, F. Li, F. K. Xiao, N. Zhao, W. Wei, L. S. Zhong and Y. H. Sun, *Catal. Today* 2012, **194**, 9-15.

43. F. Arena, G. Italiano, K. Barbera, S. Bordiga, G. Bonura, L. Spadaro and F. Frusteri, *Appl. Catal., A* 2008, **350**, 16-23.

44. B. J. A. Miller, M. A. Martin-luengo, M. S. W. Vong, Y. Wang, V. A. Self, S. M. Chapman and P. A. Sermon, *J. Mater. Chem.* , 1997, **7**, 2155-2160.

45. Enrico E. Ortrlli, J. M. Weigel, A. Wokaun., *Catal. Lett.* , 1998, **54**, 41-48.

46. C. Yang, Z. Ma, N. Zhao, W. Wei, T. Hu and Y. Sun, *Catal. Today,* 2006, **115**, 222-227.

47. G. Q. L. Xin-Mei Liu, Zi-Feng Yan, and Jorge Beltramini, I*nd.Wng.Chem.Res.,* 2003, **42**, 6518-6530.

RSC Advances Accepted Manuscript